

1 **Predicting infrasound transmission loss using deep learning**

2 Quentin Brissaud [<https://orcid.org/0000-0001-8189-4699>],¹ Sven
3 Peter Näsholm [<https://orcid.org/0000-0001-9107-4002>],^{1,2} Antoine
4 Turquet [<https://orcid.org/0000-0003-1920-935X>],¹ and Alexis Le Pichon
5 [<https://orcid.org/0000-0001-6531-069X>]³

6 ¹*NORSAR, Gunnar Randers vei 15, Kjeller, Norway*

7 ²*Department of Informatics, University of Oslo, P.O. Box 1080, NO-0316 Oslo,*
8 *Norway*

9 ³*CEA, DAM, DIF, F-91297 Arpajon, France*

10 (Dated: May 6, 2022)

SUMMARY

11
12 Modelling the spatial distribution of infrasound attenuation (or transmission loss,
13 TL) is key to understanding and interpreting microbarometer data and observations.
14 Such predictions enable the reliable assessment of infrasound source characteristics such
15 as ground pressure levels associated with earthquakes, man-made or volcanic explosion
16 properties, and ocean-generated microbarom wavefields. However, the computational
17 cost inherent in full-waveform modelling tools, such as Parabolic Equation (PE)
18 codes, often prevents the exploration of a large parameter space, i.e., variations in
19 wind models, source frequency, and source location, when deriving reliable estimates
20 of source or atmospheric properties – in particular for real-time and near-real-time
21 applications. Therefore, many studies rely on analytical regression-based heuristic
22 TL equations that neglect complex vertical wind variations and the range-dependent
23 variation in the atmospheric properties. This introduces significant uncertainties in
24 the predicted TL. In the current contribution, we propose a deep learning approach
25 trained on a large set of simulated wavefields generated using PE simulations and
26 realistic atmospheric winds to predict infrasound ground-level amplitudes up to 1000
27 km from a ground-based source. Realistic range dependent atmospheric winds are
28 constructed by combining ERA5, NRLMSISE-00, and HWM-14 atmospheric models,
29 and small-scale gravity-wave perturbations computed using the Gardner model. Given
30 a set of wind profiles as input, our new modelling framework provides a fast (0.05 s
31 runtime) and reliable (~ 5 dB error on average, compared to PE simulations) estimate
32 of the infrasound TL.

33 **Keywords:** Infrasound, Wave propagation, Machine learning, Numerical modelling

34 1. INTRODUCTION

35 Surface and subsurface sources (e.g., explosions, microbaroms, earthquakes) excite low-
36 frequency acoustic waves, i.e., infrasound, that can travel large distances in the Earth's
37 atmosphere. The refraction and reflection of infrasound waves back to the surface due
38 to vertical and horizontal gradients of atmospheric winds and temperatures enable their
39 detection at ground arrays. Because infrasound waves carry information about the source,
40 they have traditionally been used to retrieve location and yield estimates of nuclear explosions
41 (*Evers and Haak, 2010*). Recently, the detection and modelling of infrasound phases have
42 also enabled the inversion of critical seismic source and subsurface parameters such as focal
43 mechanism (*Shani-Kadmiel et al., 2021*), focal depth (*Averbuch et al., 2020; Lai et al., 2021*),
44 ground motions (*Hernandez et al., 2018*), or seismic velocity structures (*Brissaud et al.,*
45 *2021*).

46 Accurately predicting the spatial distribution of infrasound attenuation, i.e., Transmission
47 Loss (TL), is key to build robust estimates of source and subsurface characteristics. Parabolic
48 Equations (PE) (*Waxler et al., 2021*) or finite difference codes (*de Groot-Hedlin, 2008;*
49 *Brissaud et al., 2016*) are typically used to compute accurate estimates of acoustic amplitudes
50 in realistic wind structures. However, owing to the prohibitive computational cost of full-
51 waveform numerical modelling tools, most infrasound studies rely on empirical equations
52 to relate infrasound amplitudes to source parameters. Widely-used regression equations
53 include models to estimate the explosion yield from peak infrasound amplitudes (e.g., *Golden*
54 *et al., 2012*) and empirical equations relating pressure at the source and observed infrasound
55 amplitudes (*Le Pichon et al., 2012*). In particular, the construction of empirical equations
56 ignores or greatly over-simplifies atmospheric wind structures. For instance, in *Le Pichon*
57 *et al. (2012)*, the authors assume a single range-independent Gaussian stratospheric duct
58 to optimize their regression model. Yet, vertical and horizontal wind gradients at various
59 altitudes can drastically affect the TL at the ground (*de Groot-Hedlin et al., 2010*).

60 Empirical models rely on over-simplistic representations of the wind structures because the
61 mapping between source frequency, atmospheric specifications, and TL is highly nonlinear
62 and poorly constrained. In order to bridge the gap between computationally expensive

63 numerical models and over-simplistic empirical equations, supervised Machine-Learning (ML)
 64 models trained over synthetic or recorded datasets can offer an accurate and inexpensive
 65 alternative to existing modelling tools (*Michalopoulou et al.*, 2021). Previous studies have
 66 employed ML models to predict TL: *Pettit and Wilson* (2020) built a Physics-Informed
 67 Neural Network (PINN) trained over synthetic PE simulation results to predict attenuation
 68 maps (along range and altitude) in the atmospheric boundary layer. PINN introduces
 69 regularization terms in the cost function to account for physics-based constraints. This model
 70 provides an inexpensive alternative to existing modelling tools but shows low accuracy as
 71 it struggles with adjusting the weights of the physics-informed parameters in the objective
 72 function. Additionally, atmospheric specifications are encoded using only wind profiles,
 73 and this approach was not adapted to long-range propagation. *Hart et al.* (2021) used a
 74 fully connected neural network to predict two-dimensional (2D) attenuation in a turbulent
 75 atmosphere from a set of predefined input parameters describing the turbulent field. This
 76 model shows a relatively low error (< 7 dB) but relies on over-simplified wind models with
 77 a set of 13 inputs to describe the velocity field which are not representative of long-range
 78 propagation.

79 Relating wind structures to TLs is key to accurately reproduce full-waveform simulations.
 80 Instead of using pre-defined parameters to describe the wind velocity field, Convolutional-
 81 Neural Networks (CNN, *Krizhevsky et al.* (2012)) provide an excellent solution to identify
 82 patterns of interest within input wind models. Such patterns are extracted using a set of
 83 filters described by a number of coefficients that are optimized during the ML training process.
 84 Such network is generally followed by a set of fully-connected layers relating the encoded
 85 information by the CNN and the output. In this contribution we propose a new ML model
 86 trained over synthetic PE simulations to build ground TL in realistic range-dependent wind
 87 models that both shows a low computational cost compared to existing modelling tools, and
 88 high accuracy over long-range propagation.

89 2. BUILDING A TRANSMISSION-LOSS DATASET

90 Building a synthetic TL dataset requires a modelling tool and a set of atmospheric models.
 91 Similar to *Le Pichon et al. (2012)*, we generate TL profiles using the open-source (PE) solver
 92 ePape, provided by the US National Center for Physical Acoustics (NCPA, *Waxler et al.*,
 93 2021). To provide realistic bounds for the atmospheric models, we collect 1048 slices of 1000
 94 km length up to 80 km altitude from ERA5 re-analysis models, discretized over 137 altitude
 95 levels (*ECMWF, 2018*) with a horizontal resolution of 1 degree. The choice of 1000 km slice
 96 length enables the analysis of a wide variety of regional observations (e.g., *Ceranna et al.*,
 97 2009; *Fee and Matoza, 2013*) while keeping the computational time low to build the training
 98 dataset. The spatial step of 1 degree is picked as a trade-off between the resolution to capture
 99 ERA5 spatial variability and the computational time to both download atmospheric models
 100 and run simulations. Since ERA5 models are limited to around 80 km altitude, we use
 101 two empirical models to retrieve atmospheric properties up to 120 km altitude: HWM-14
 102 to obtain zonal and meridional winds (*Drob et al., 2015*), and NRLMSISE-00 to retrieve
 103 temperatures (*Picone et al., 2002*). ERA5 and HWM-14/NRLMSISE-00 atmospheric models
 104 are stitched together using a cubic interpolation over the altitude range of 75 to 85 km.
 105 Because atmospheric properties vary with latitude, longitude, and time of the year, ERA5
 106 profiles are uniformly sampled between latitudes -40 to 70 degrees, longitudes -150 to 165
 107 degrees, and between years 2010 to 2020 (see Fig. 1a).

108 ERA5 models lack resolution to capture fine-scale wind and temperature fluctuations
 109 such as gravity-wave breaking above the troposphere (*Chunchuzov et al., 2015; Chunchuzov*
 110 *and Kulichkov, 2019*). To account for unresolved wind perturbations at higher altitudes,
 111 infrasound studies typically consider the Gardner model to add gravity-wave perturbations
 112 to the original wind profiles (*Gardner et al., 1993*). Therefore, we account for small-scale
 113 perturbations by considering four Gardner realizations for each atmospheric slice in addition
 114 to the original slice (see green stage in Fig. 2a). Similar to *Norris and Gibson (2002)*, we
 115 generate Gardner perturbations by considering four altitude levels 84, 70, 45, and 21 km, at
 116 which we sample standard deviations uniformly within the range of, respectively, 1–25, 1–18,
 117 1–10, and 1–5 m/s. Finally, because the direction of propagation within an atmospheric slice,

118 i.e., upwind or downwind propagation, greatly alters the TLs at the ground, we augment
 119 our dataset of atmospheric models by running simulations in both scenarios by changing the
 120 sign of the projected winds (see yellow stage in Fig. 2a). Our final dataset includes 41920
 121 simulations.

122 Effective velocity ratios \bar{c}_{eff} , i.e., ratio between the maximum effective velocity in a given
 123 atmospheric layer and the surface, provide useful insight into the likelihood of infrasound
 124 refractions along the direction of propagation. Similarly to *Le Pichon et al. (2012)*, we
 125 compute \bar{c}_{eff} as $\bar{c}_{\text{eff}} = \max_{z \in \text{layer}} \{c_{\text{eff}}(z)\} / c_{\text{eff}}(z = 0)$, where $c_{\text{eff,layer}}(z) = c(z) + w(z)$ is the
 126 effective velocity, where c (m/s) is the adiabatic sound velocity, w (m/s) the along-path
 127 wind velocity, z (m) the altitude, and $\text{layer} = (z_{\text{start}}, z_{\text{end}})$ is given by the altitude bounds
 128 z_{start} and z_{end} (m) for a given atmospheric layer. The distribution of effective velocity
 129 ratios \bar{c}_{eff} computed from our final atmospheric model dataset for three different altitude
 130 regimes, shown in Fig. 1b, is close to a Gaussian distribution, centered around $\bar{c}_{\text{eff}} = 1$.
 131 This indicates that our dataset includes models with and without strong high-altitude ducts.
 132 The distribution of tropospheric effective velocity ratios is narrower than for higher-altitude
 133 layers. This owes to the small number of occurrences of tropospheric wave ducts in our
 134 dataset. In addition to vertical variations of atmospheric properties, lateral variations can
 135 play a significant role for long-range infrasound propagation. We quantify the range of lateral
 136 variations by computing the maximum lateral standard deviation of wind velocities in a given
 137 atmospheric layer $\text{std}_{\text{layer}}$ (m/s) such that $\text{std}_{\text{layer}} = \max_{z \in \text{layer}} (\text{std}_{x \in \text{range}} \{w(x, z)\})$, where
 138 std is the standard deviation, $w(x, z)$ (m/s) is the along-path wind at a given range x (m)
 139 and altitude z (m), $\text{range} = (0, 1000)$ km is the total atmospheric slice range. In contrast to
 140 large vertical variations of wind velocities, most ERA5 models show small lateral variations
 141 of wind velocities ($\text{std}_{\text{layer}} < 15$ m/s, see Fig. 1c). The largest lateral wind variations occur
 142 above the stratosphere since winds at these high altitudes are generally the strongest on
 143 Earth (*Blanc et al., 2018*).

144 TL profiles are then computed over 1000 km from the source for a source at ground
 145 level using 7 Padé coefficients and the Sutherland-Bass attenuation model (*Sutherland*
 146 *and Bass, 2004*) using NCPA's ePape PE simulator (*Waxler et al., 2021*). We extract 10
 147 atmospheric profiles along each 1000 km slice, i.e., 100 km horizontal discretization, from

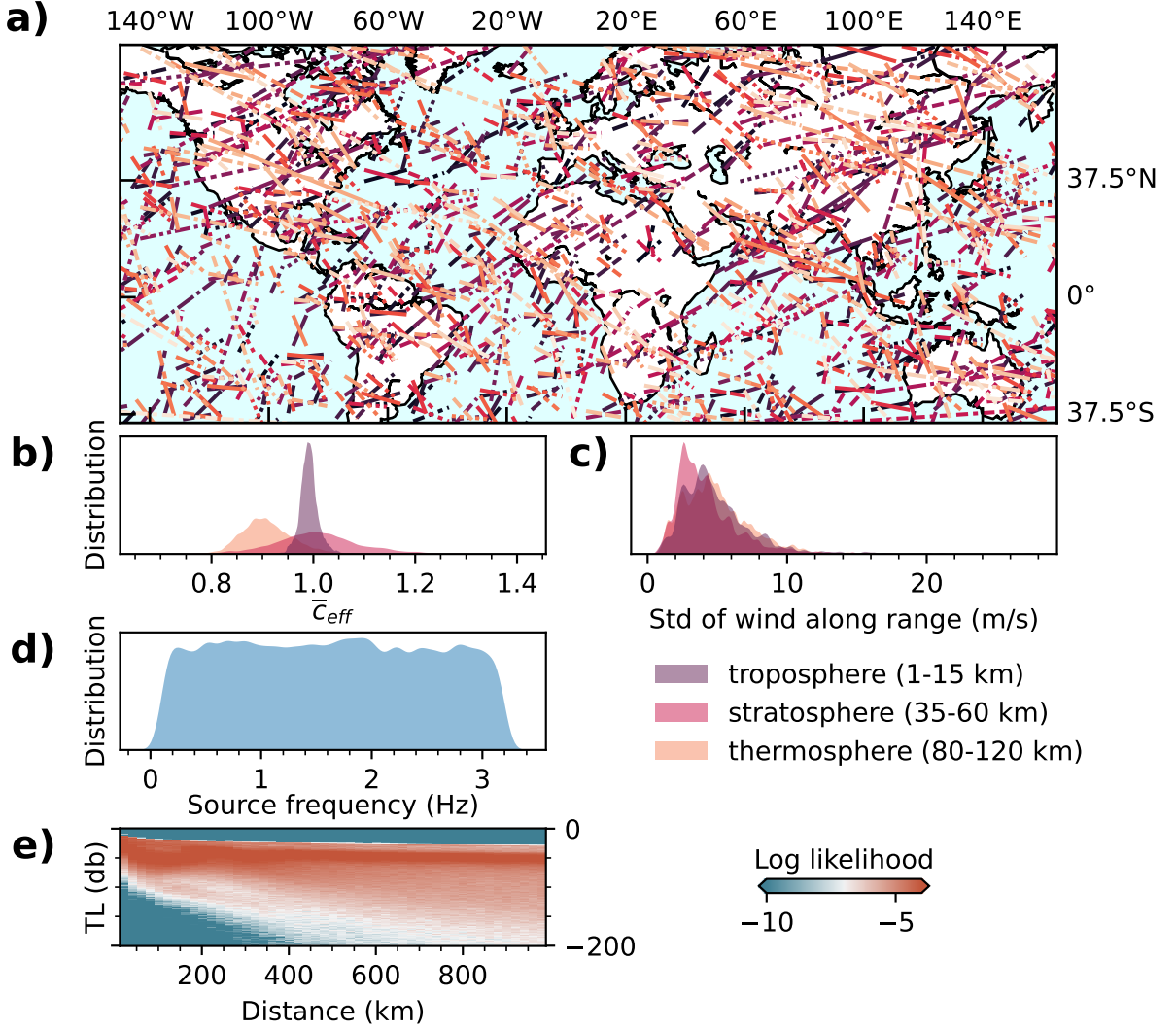


Figure 1. Atmospheric model and TL datasets. (a) distribution of 1000 km long atmospheric slices extracted from the ERA5 dataset. Slices are given different colors and line styles (dashed and solid lines) to facilitate the visualization of their distribution around the globe. (b) Distribution of effective velocity ratio \bar{c}_{eff} between the ground and various atmospheric layers: troposphere (purple) between 1 and 15 km altitude, troposphere (purple) between 35 and 60 km altitude, and thermosphere (purple) between 80 and 120 km altitude. (c) Distribution of standard deviations of wind velocities along range for various atmospheric layers. (d) Distribution of input source frequencies used in PE simulations to build the entire TL dataset. (e) TL distribution represented as log likelihood (computed from Gaussian Kernel density estimates) vs distance determined from our entire TL dataset.

148 the ERA5 dataset. Signals from sources of interest (earthquakes, volcanoes, large explosions)
 149 typically show dominant frequencies below 5 Hz. Therefore, similar to *Le Pichon et al.*
 150 (2012), we sample 5 source frequencies from a uniform distribution between 0.1 to 3.2 Hz
 151 for each atmospheric slice (see Fig. 1d and Fig. 2a). PE assumes slow lateral variations in
 152 the atmospheric properties over the scale of one wavelength. To ensure smoothly varying
 153 atmospheric properties, we must only consider models that do not include lateral variations
 154 over the scale of the largest wavelength considered, which means $\lambda \approx 3.5$ km at 0.1 Hz.
 155 Because we are using a 100 km horizontal discretization, interpolation of atmospheric
 156 properties within the NCPA software will generate smooth-enough models to fulfil the PE
 157 assumptions. The resulting distribution of TL profiles is shown in Fig. 2e. Most profiles show
 158 TL values > -100 db at large distances from the source owing to the presence of Gardner
 159 perturbations in most models which refract significantly the infrasound energy back to the
 160 surface (*Chunchuzov et al., 2015*).

161 PE neglect nonlinear terms and cross-winds. Nonlinearities affect primarily the amplitude
 162 and frequency content of thermospheric phases for large-amplitude pressure sources (*Sabatini*
 163 *et al., 2019*). Therefore, uncertainties on the predicted amplitudes must be accounted for when
 164 investigating high-yield surface sources. When large-amplitude sources are considered, PE
 165 simulations will severely overpredict the amplitude of refracted phases at the ground. While
 166 cross-winds have a significant impact on the apparent backazimuth observed from refracted
 167 phases at stations located at large distances from the source, their influence on infrasound
 168 amplitudes is generally considered insignificant (*Hernandez et al., 2018; Shani-Kadmiel et al.,*
 169 *2021*).

170 3. DESIGNING A TRANSMISSION-LOSS MODEL

171 PE based simulations are often used to provide a mapping between 2D range-dependent
 172 profiles (temperature, winds, and pressure), frequency, and transmission loss profiles under
 173 the effective-velocity approximation. Our goal is to retrieve the same TL estimates as
 174 provided directly by PE, but at a significantly reduced computational cost. This is achieved
 175 using an alternative nonlinear map between the atmospheric specification and frequency

176 inputs and the TL output using a neural network which is pre-trained on an extended set of
 177 PE simulations. Variations of surface-to-surface TL with range for a given source frequency
 178 between different atmospheric models are primarily controlled by lateral and vertical wind
 179 variations. To reduce the ML architecture complexity, we assume a nonlinear mapping to
 180 exist between frequency, 2D wind, and TL and that this adequately approximates the full
 181 PE solution.

182 We implement this mapping between winds and ground TLs using a supervised deep
 183 learning algorithm. A deep learning neural network maps a set of inputs, e.g., wind profiles
 184 and frequency, into a set of outputs, e.g., TL profiles. For a given network architecture,
 185 supervised learning consists of the optimization of hierarchically organized nonlinear functions.
 186 The optimization process iteratively updates the non-linear function parameters by comparing
 187 training outputs and outputs predicted by the deep learning model. The most generic network
 188 consists of a succession of fully-connected layers where each layer is composed of a set of
 189 nonlinear functions described by a weight, a bias, and an activation function. For fully-
 190 connected layers, the output of each function from a first layer is used as input to each
 191 function of the next layer. Such architecture does not assume any relationships between
 192 the inputs and outputs of successive layers. This generic layer configuration leads to lower
 193 predictive power, as it requires an extended number of parameters to optimize and ignores
 194 spatial correlations in the input data.

195 Accounting for spatial correlations, i.e., relationships between neighboring inputs such as
 196 local wind gradients, are key to extract physically-meaningful patterns from continuous input
 197 data (e.g., images or timeseries) and improve network performances (*d'Ascoli et al.*, 2019). To
 198 leverage spatial correlations, Convolutional Neural Networks (CNN) use a series of operations,
 199 namely, digital filtering, pooling, and activation (see blue stage in Fig. 2b) to extract patterns
 200 at different scales across 1D or 2D input data (*Krizhevsky et al.*, 2012). In 2D, the digital
 201 filtering step consists of the convolution product between a series of kernel and the input
 202 image which outputs a filtered image. During the training of a CNN, the optimization process
 203 will update the values, or parameters, that compose the kernels (e.g., 25 parameters for a 5×5
 204 kernel). Pooling consists of the downsampling of the inputs by typically computing averages
 205 or determining the maximum of the filtered image. This downsampling step reduces the

206 number of parameters to train and makes the model more robust to variations in the position
207 of the features (i.e., wind patterns here) in the input image. CNNs generally outperform
208 fully-connected networks for both regression and classification tasks owing to their efficient
209 pattern extraction stage (*d'Ascoli et al.*, 2019).

210 The infrasound refraction process can be seen as the cumulative effect of successive wind
211 heterogeneities, i.e., wind patterns, along the propagation path bending the rays back to
212 the surface (*Chunchuzov et al.*, 2015). CNNs are excellent choices when extracting wind
213 patterns and encoding the nonlinear relationship between wind patterns and ground TLs.
214 We therefore use a CNN architecture by representing each along-path wind model, used as
215 input of PE simulators, as a one-channel 2D image, i.e., gray 2D image, where the x-axis is
216 the source range, the y-axis the altitude, and the wind amplitude the contrast. Since the
217 relationship between frequency and TL for complex wind structures is poorly constrained,
218 we approximate this undefined mapping by using fully-connected layers, which make no
219 assumptions about the input spatial correlations. The final architecture (Fig. 2b) consists
220 of two layers of 2D convolutions using 5×5 kernels (i.e., smallest filters with size 100×15
221 km) followed by Batch normalization and Average Pooling. The encoded winds are then
222 concatenated with the source frequency input, and three fully-connected layers. Average
223 pooling consists of taking the average of the output of each convolution which is employed to
224 both reduce the dimensionality and learn translation invariance over the input representation.
225 Batch normalization (*Ioffe and Szegedy*, 2015) re-centers and re-scale the input of each layer
226 over each mini-batch during the training process. Normalizing batches reduces the variations
227 of distributions in inputs at each layer, speeds up training, and produces more reliable models.
228 Both Batch normalization and Average Pooling layers are used to make the ML model more
229 robust to new data. The last fully connected layer consists of the output layer that represents
230 the normalized TL profile between 0 to 1000 km. All weights are initialized using a uniform
231 Glorot initializer (*Glorot and Bengio*, 2010).

232 To facilitate the recognition of patterns in input data, winds are vertically downsampled and
233 horizontally upsampled from a 10×1000 2D image, i.e., 10 profiles discretized over 1000 points
234 along the altitude, to a 50×40 2D image. To limit the range of input and output values,
235 input profiles and output TLs are then normalized by removing the mean and scaled to unit

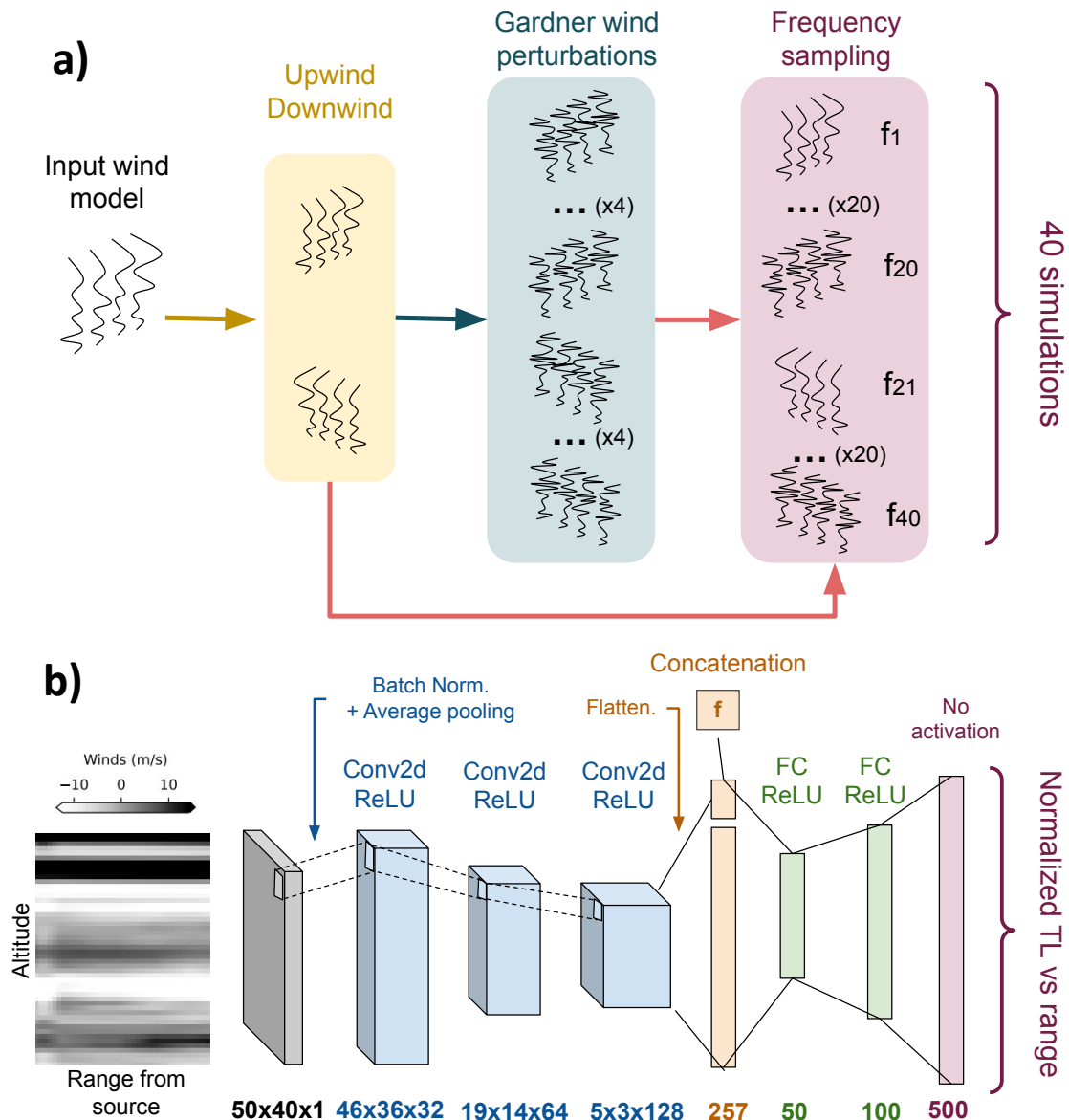


Figure 2. Ground-truth dataset creation and ML architecture. (a) Procedure to augment our atmospheric model dataset. First upwind and downwind scenarios are considered for each wind slice. The difference between upwind and downwind scenarios corresponds simply to flipping the sign of the projected winds onto the slice. Then, 5 random set of Gardner perturbations are generated for both upwind and downwind scenarios. Finally, 4 input frequencies are considered for each perturbed wind model. A total of 40 wind models are generated for each atmospheric slice extracted from the ERA5 dataset. (b) Cartoon depicting a deep learning network workflow for TL predictions. We use 2D representation of wind amplitudes (grey) with size 50×40 as inputs for our ML model. In the first stage (blue) we use three 2d Convolutional layers (Conv2d) to encode the wind information as a vector of size 256. In the second stage (orange), we concatenate this wind encoding with the input source frequency. In the third stage (green), we build a mapping between input frequency and encoded wind representation using two Fully-Connected (FC) layers to finally produce a normalized TL vs range of size 500 (red). This normalized TL can be transformed back to dB by using the

236 variance. Both mean and variance are computed over the training dataset only. The output
 237 layer corresponds to the normalized TL profile linearly interpolated over 500 points within
 238 the range 0 to 1000 km. We train the neural network using an Adam optimizer (*Kingma*
 239 *and Ba*, 2015) with a starting learning rate of 10^{-4} . ReLu activation functions are used
 240 throughout the network expect for the output layer where we do use any activation function.
 241 The ML architecture is implemented in Python using the TensorFlow library (*Abadi et al.*,
 242 2015). More details about architecture optimization are provided in Appendix A.

243 4. VALIDATION OF MACHINE-LEARNING PREDICTIONS

244 To optimize our ML model, we split our full dataset between 85% training data and 15%
 245 validation data. Strong correlations in TL are expected between PE simulations using wind
 246 models corresponding to perturbed versions of the same original unperturbed wind model
 247 along a given atmospheric slice. Therefore, before training, all simulations corresponding
 248 to the same original atmospheric slice (see the first stage in Fig. 2a) are added to same set
 249 (either training or validation) to make our model more robust to new data. To facilitate
 250 convergence, we adaptatively update the learning rate when the Root Mean-Square-Error
 251 (RMSE) does not decrease over the course of 3 epochs, i.e., training steps. RMSE is computed
 252 as $RMSE = \sqrt{(1/N) \sum_{i=1,N} |TL_{PE}^i - TL_{ML}^i|^2}$, where $i \in (1, N)$ is the simulation index in the
 253 test dataset, N the size of the test dataset, TL_{PE} is the TL profile predicted with PE, and
 254 TL_{ML} is the TL profile predicted with ML. To avoid over-fitting the training data, we use
 255 early stopping if the MSE does not decrease over the course of 12 epochs. Finally, to speed
 256 up the training process and improve generalization, we use mini-batches of size 32.

257 We evaluate the performances the ML architecture by training our model over five folds,
 258 i.e., five different splits between training and testing datasets. The ML model converges
 259 within 65 epochs for our best fold with a validation RMSE (over normalized TL profiles)
 260 twice larger than the training RMSE (see Fig. 3a). Once trained, the ML model has a
 261 computational cost of around 0.05 s (Dell T5610 Intel Xeon E5-2630 v2 2.6 GHz 6 CPUs
 262 64GB RAM on CentOS 7) for all input frequencies. Over the same frequency range, PE
 263 simulation cost increases significantly with frequency, up to 100 s at 3.2 Hz (see Fig. 3b),

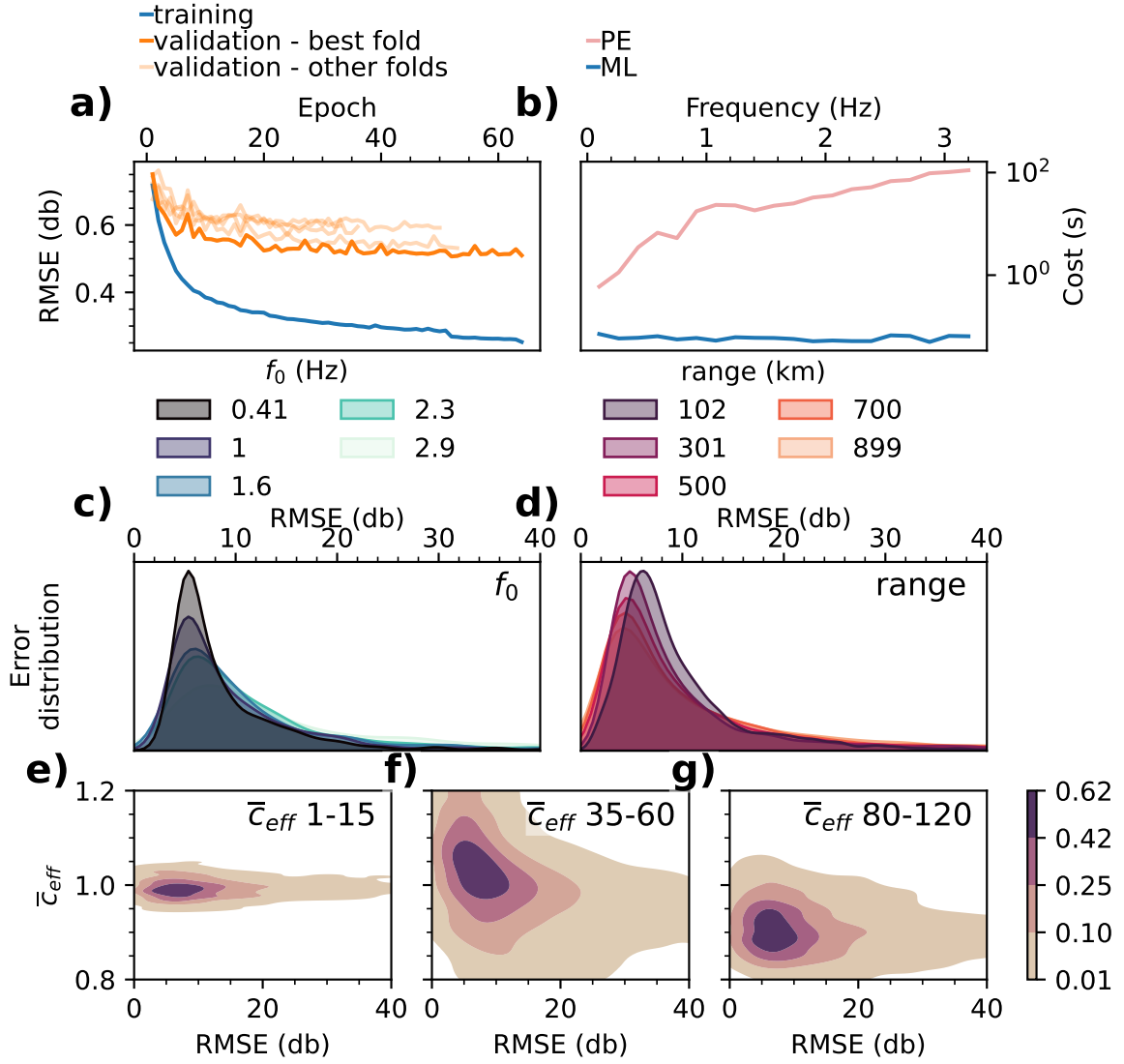


Figure 3. Training and validation of the ML model. (a) Evolution of Root-Mean Square Errors (RMSE) with training epoch for different training (blue) and validation (orange) folds. The fold with best final accuracy is shown as a thick orange line. (b) Computational cost of PE simulations (red) and ML predictions (blue) vs input source frequencies. (c) Distribution of RMSE over the testing dataset for various input frequencies. (d) Distribution of RMSE over the testing dataset for various ranges from the source. (e-g) Distribution of RMSE over the testing dataset for various values of effective velocity ratio \bar{c}_{eff} in (e) the troposphere, (f) the stratosphere, and (g) the thermosphere.

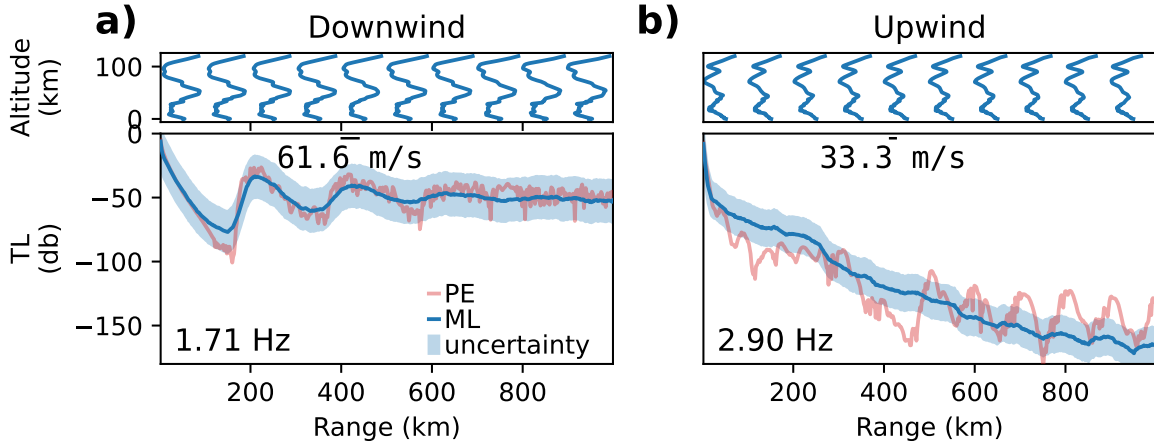


Figure 4. TL predicted by PE simulations (red) and ML model (blue) along with the ML uncertainty (light blue) for a (a) downwind and an (b) upwind scenario. Top, corresponding range-dependent effective velocity models. The ML uncertainty u is computed, in a given frequency range \mathbf{f} , as the standard deviation of TL errors vs range from the source over the testing dataset such that $u(r, \mathbf{f}) = \text{std}\{|\text{PE}(r, f) - \text{ML}(r, f)|\}$, where r is the range, f is the frequency, PE is the TL predicted using Parabolic Equations, and ML is the TL predicted using Machine Learning.

264 which is 2000 times larger than the cost for a ML prediction. In Figs 3c and 3d, we show
 265 that the RMSE of our ML model follows a bell-shaped distribution centred between 5 to 9
 266 dB with both variations in distance from the source and source frequency. This distribution
 267 of errors indicates that our ML implementation is stable for the range of frequencies and
 268 distances considered in our dataset. Larger errors tend to occur for high frequencies (> 2
 269 Hz) and close to the source (< 200 km). Higher frequencies are more sensitive to small-scale
 270 wind variations which leads to more complex distributions of TL with range. This added
 271 complexity in high-frequency TLs leads to larger errors in ML predictions. Most TL variations
 272 occur within 200 km from the source with the presence of the first acoustic shadow zone and
 273 first stratospheric return which explains the larger errors observed close to the source. Errors
 274 are also stable with variations in effective velocity ratios in different atmospheric layers (Figs
 275 3efg).

276 We observe in Figs 4a and 4b that ML predictions match well the average variations of
 277 TL with range from the source. In particular, the ML model captures accurately the TL gain

278 associated with the different stratospheric returns and the TL asymptotic behaviour at large
 279 distances from the source. However, the ML model does not fully reproduce high-frequency
 280 TL variations, which owe to vertical and horizontal atmospheric model variations including
 281 small-scale changes in effective wind velocities. The ML model therefore provides a low-passed
 282 solution of the true TL profile. Our model is unable to learn the entire mapping between
 283 atmospheric model heterogeneities and TLs primarily due to both the downsampling of
 284 wind profiles and the lack of training data. Yet, large uncertainties are present in currently
 285 available atmospheric models, in particular above the troposphere where small-scale wind
 286 and temperature perturbations are generally unresolved. Therefore, these high-frequency TL
 287 oscillations generally fall within the uncertainty range associated with available atmospheric
 288 model resolutions. Along with ML predictions, we can determine an estimate of the ML
 289 uncertainty u by computing the standard deviation of TL errors vs range in a given frequency
 290 range \mathbf{f} , as the standard deviation of TL errors vs range from the source over the testing
 291 dataset such that $u(r, \mathbf{f}) = \text{std}\{|\text{PE}(r, f) - \text{ML}(r, f)|\}$, where r is the range, f is the frequency,
 292 PE is the TL predicted using Parabolic Equations, and ML is the TL predicted using Machine
 293 Learning. The frequency dependence of the uncertainty curves u (see error distribution vs
 294 frequency in Fig 3c) is accounted for by computing the errors in five frequency ranges \mathbf{f}
 295 equally distributed between 0.1 to 3.2 Hz. We observe that errors between our ML predictions
 296 and the PE simulations generally fall within the ML uncertainty range (blue shaded region in
 297 Figs 4a and 4b). As suggested by the distributions shown in Figs 3c and 3d, the uncertainty
 298 range remains stable with variations in frequency and range from the source.

299 5. ANALYTICAL VS ML PREDICTIONS OF GROUND TLS

300 Stratospheric winds are one of the dominant factors to explain the refraction of acoustic
 301 waves at large distances from the source (*de Groot-Hedlin et al.*, 2010). A widely used
 302 empirical regression equation, introduced in *Le Pichon et al.* (2012), referred in the rest of the
 303 paper as LP12, has provided estimates of TL over large distances from a variety of surface
 304 sources (*Hernandez et al.*, 2018; *Vorobeva et al.*, 2021; *De Carlo et al.*, 2021). However,
 305 the original model was optimized over a set of idealized synthetic and range-independent

306 models where the main feature was a stratospheric duct of various strength, modelled using
 307 a Gaussian wind profile centered at 50 km altitude added to the U.S. Standard Atmosphere.

308 Estimates of LP12 uncertainties over idealized range-independent profiles (*Tailpied et al.*,
 309 2021) show low errors compared to PE simulations (< 10 dB) when strong winds are ducting
 310 the signal in the stratosphere. However, in the case of upwind propagation, the accuracy
 311 decreases significantly, especially at high frequencies where the errors can be up to 70 dB.
 312 Yet, uncertainties introduced by this empirical model for realistic range-dependent wind
 313 models are still mostly unconstrained. Comparisons with our PE simulation dataset offer
 314 the opportunity to investigate the uncertainties associated with highly heterogeneous wind
 315 models for both LP12 and our ML model.

316 A typical approach to investigate the influence of stratospheric winds on refracted infra-
 317 sound is to represent the variations of TLs with variations in stratospheric effective velocity
 318 ratios, i.e., stratospheric wind strength, and range from the source for different frequencies
 319 (*Le Pichon et al.*, 2012). Yet, in contrast to the dataset used for the optimization of LP12,
 320 effective velocity ratios in our dataset are not equally distributed since we use the atmospheric
 321 model products and not idealized profiles. To provide meaningful comparisons with LP12,
 322 we build uniformly-spaced 2D TL maps by performing a linear interpolation of the ML-
 323 and PE-predicted TLs between $0.85 \leq \bar{c}_{\text{eff}, 35-60 \text{ km}} \leq 1.2$, where $\bar{c}_{\text{eff}, 35-60 \text{ km}}$ is the effective
 324 velocity ratio between 35 to 60 km altitude. Linearly-interpolated TL maps are shown in
 325 Fig. 5. Comparison between Figs 5a and 5b as well as between Figs 5e and 5f shows that the
 326 PE-based TL is well-reproduced by ML for the two frequencies considered. As mentioned
 327 earlier, our ML model tends to smooth out the rapid oscillations in TL predicted by PE
 328 simulations. Yet, average errors shown in Figs 5c and 5g are stable around 5 dB for all values
 329 of $\bar{c}_{\text{eff}, 35-60 \text{ km}}$.

330 We also observe that LP12, represented as isocontours in Figs 5b and 5f, is able to capture
 331 the main features of the TL maps, namely the first acoustic shadow zone and first stratospheric
 332 return within 250 km from the source, and the high attenuation for low stratospheric effective
 333 velocity ratios ($\bar{c}_{\text{eff}, 35-60 \text{ km}} < 1$). The good agreement between numerical simulations and
 334 LP12 (Figs 5b and 5f) suggests that average TLs are most sensitive to stratospheric winds
 335 when a strong duct is present. LP12 also captures well the high- $\bar{c}_{\text{eff}, 35-60 \text{ km}}$ trends of median

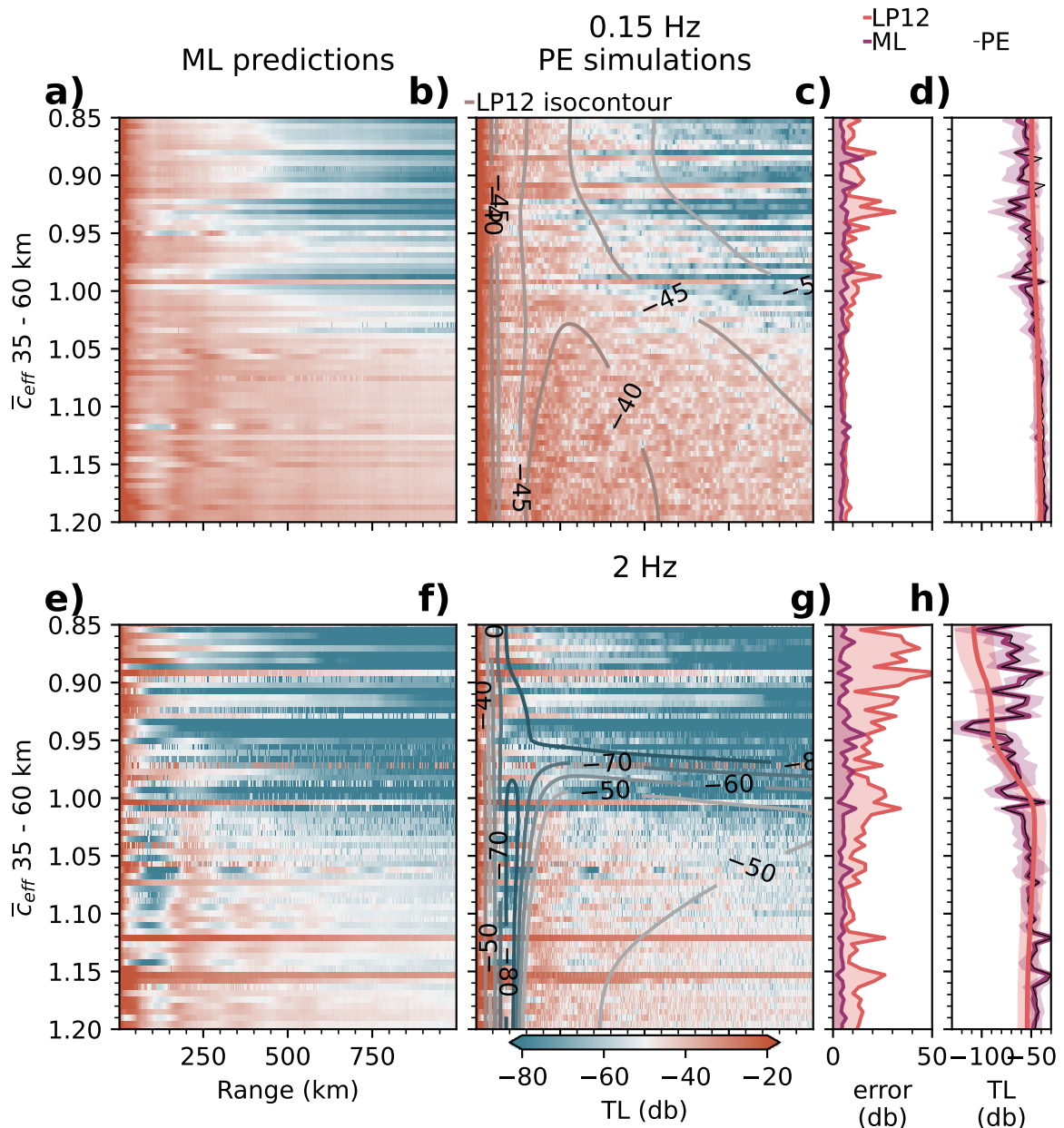


Figure 5. Comparisons of TL maps produced by PE, ML, and LP12 models. (a,b) and (e,f) TL maps vs range and effective velocity ratio \bar{c}_{eff} between 35 – 60 km altitude for a source frequency at 0.15 Hz (a,b) and at 2 Hz (e,f) as predicted by (a,e) the ML model, (b,f) PE simulations, and (b,f isocontours) Le Pichon model. (c,g) RMSE in dB between the interpolated TL maps from the PE simulations and the ML model (purple) and Le Pichon model (LP12, red) at (c) 0.15 Hz and (g) 2 Hz. (d,h) Median TL in dB vs $\bar{c}_{eff, 35-60 km}$ computed from the interpolated TL maps from the PE (black), the ML (purple), and LP12 (red) models at (f) 0.15 Hz and (h) 2 Hz.

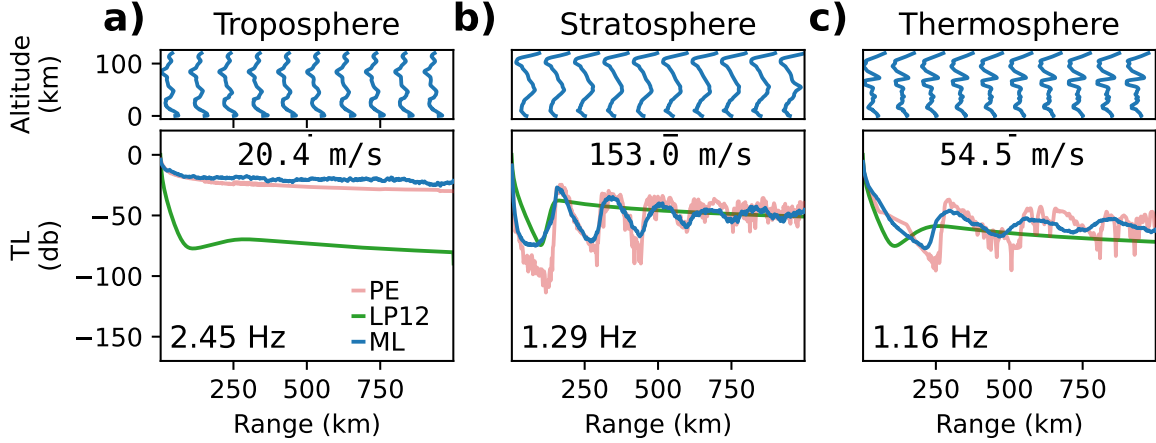


Figure 6. TL predicted by PE simulations (red), LP12 (green), and ML model (blue) for a wind model with a (a) tropospheric duct, (b) stratospheric duct, (c) thermospheric duct, and (d) strong upwind conditions in the stratosphere. (a-d) top, effective velocity profiles used for PE predictions.

336 TLs (Figs 5d and 5h). However, errors between LP12 and PE simulations increase significantly
 337 for low stratospheric effective velocity ratios ($\bar{c}_{\text{eff}, 35-60 \text{ km}} < 1$).

338 LP12 systematically underpredicts TLs for low effective velocity ratios at high frequencies
 339 (Fig. 5g), which is consistent with a previous assessment of the empirical model (*Tailpied et al.*,
 340 2021). This owes primarily to the presence of wind ducts outside the stratosphere that are
 341 not accounted for in the polynomial parametrization of the empirical model). LP12's errors
 342 are particularly strong at high frequencies (*Chunchuzov et al.*, 2015) and close to the source
 343 where small wind variations can make acoustic energy return to the ground (*Chunchuzov*
 344 *et al.*, 2015).

345 The influence of various ducting conditions on ML and LP12 predictions are further
 346 illustrated in Figure 6. LP12 captures well the first acoustic shadow zone as well as the
 347 asymptotic TL trend at large distance from the source (Figure 6b). However, the error
 348 between PE and LP12 increases significantly when a tropospheric or a thermospheric duct
 349 are present (Figure 6ac). In particular, tropospheric ducted arrivals generally show strong
 350 acoustic amplitudes at ground arrays and can represent up to 20% of the energy radiated
 351 from the source (*Drob et al.*, 2003). Accounting for tropospheric ducting is therefore critical
 352 for accurate attenuation assessments in the range of distances from the source ($< 1000 \text{ km}$)

353 considered here. However, these ducts generally exist only up to a range of ~ 750 km and
 354 generally do not affect longer-range propagation at a global scale (*Drob et al.*, 2003). Still,
 355 under certain circumstances the tropospheric ducting can be extended as demonstrated,
 356 e.g., both in simulations and data recordings at beyond 1600 km range from the Sayarim
 357 infrasound calibration experiments (*Fee et al.*, 2013), as well as up to 1000 km from the
 358 Antares rocket explosion (*Vergoz et al.*, 2019). For example, a strong tropospheric tailwind
 359 direction jet can enhance the tropospheric waveguide.

360 6. CONCLUSIONS AND DISCUSSION

361 In this contribution we have proposed an ML-based approach to rapidly (~ 0.05 s runtime)
 362 and reliably (~ 5 db dB error on average, compared to PE simulations) predict estimates
 363 of ground TL from surface sources up to 1000 km. The trained ML model takes as input a
 364 range-dependent atmospheric specification and a wave frequency to generate a TL estimate.
 365 Errors compared to full PE simulations remain low for increasing source frequency at close
 366 range of the source. Our ML model can reproduce complex TL where guided tropospheric
 367 waves and multiple stratospheric returns are present. Comparisons with the regression
 368 equation introduced in *Le Pichon et al.* (2012) indicate that considering only the influence
 369 of stratospheric winds between 35 and 60 km altitude enables one to reproduce the main
 370 features of the variations of TL with effective velocity ratio (LP12's errors remain below 10
 371 dB at low frequency for $\bar{c}_{\text{eff}} > 1$). However, by neglecting the impact of tropospheric and
 372 high-altitude winds, LP12 can lead to significant errors (RMSE ~ 50 dB) while the ML
 373 model is able to capture accurately the TL for highly heterogeneous wind structures.

374 Several techniques could be used to further improve the accuracy of our ML model.
 375 Running additional simulations will increase the size of the training dataset which will reduce
 376 the RMSE but will not affect the computational cost of ML predictions once trained. Building
 377 on *Raissi et al.* (2019); *Pettit and Wilson* (2020), physical constraints imposed by the PEs
 378 and its boundary conditions could be integrated into the cost function to facilitate the
 379 convergence of our ML model. Because we trained our algorithm over atmospheric models
 380 extracted only from the ERA5 and the NRLMSISE-00/HWM-14 climatological models,

381 biases might be present in the structure of the input wind fields used for training due to
382 the specific system of equations solved to produce ERA5 models. Acquiring atmospheric
383 models from additional sources (e.g., MERRA dataset as presented in *Kumar et al. (2015)*),
384 could make the ML model more robust to arbitrary wind models. In addition to atmospheric
385 models, small-scale gravity-wave models could be enhanced by considering more realistic
386 range-dependent perturbations (*Drob et al., 2013; Lalande and Waxler, 2016*).

387 Transfer Learning (TrLe) can be used to improve the performances of CNNs over small
388 datasets (*Zhuang et al., 2020*). CNN parameters are generally initialized using somewhat
389 arbitrary distributions (such as the uniform Glorot initializer (*Glorot and Bengio, 2010*)) that
390 are not tailored to specific classification or regression problems. Because the optimization
391 process is sensitive to the initial parameter distributions (misfits typically show large numbers
392 of local minima), arbitrary distributions do not guarantee convergence. The idea behind
393 TrLe is to exploit invariances in the feature extraction process across different datasets and
394 different tasks (e.g., filters learned to extract edges in dogs vs cats classification can also be
395 used to detect cars) to facilitate the convergence of the optimization process. TrLe consists
396 of initializing a ML model using the parameters of another ML model pre-trained over a
397 different dataset and possibly for a different task. Here, we tested TrLe by assuming that
398 there are some invariances between our wind feature extraction problem and traditional
399 image-segmentation problems such as multi-class classification of real images (e.g., ImageNet
400 *Deng et al., 2009*). We tested TrLe by replacing our CNN encoding stage (blue in Fig. 2b) by
401 both a VGG16 (*Simonyan and Zisserman, 2015*) or a ResNet50 (*He et al., 2016*) network and
402 trained our network using their pre-trained weights and removing pooling layers. However,
403 TrLe's performances were worse (RMSE = 9) than with the model presented in Fig. 2b owing
404 to the significant differences between both the set of images used for training in VGG16 or
405 ResNet50 and our wind inputs and the problem of image detection vs TL prediction. .

406 Our ML model was trained over a set of simulations generated by a PE modelling tool
407 (*Waxler et al., 2021*) which has strong assumptions about infrasound propagation (see Section
408 2). In particular, a limitation of PE simulations is in the fact that it ignores cross-winds which
409 might have a strong impact on the acoustic wavefronts at large distances from the source. Yet,
410 this question remains largely unanswered in the literature and further research is needed to

411 provide robust assessments of cross-winds influence on the acoustic wavefield. Nonetheless, ML
412 predictions are expected to be significantly improved if the synthetic dataset were generated
413 using more accurate modelling tools solving the linearized Navier-Stokes equations such as
414 Finite-Differences (FD, *Brissaud et al. (2016)*; *Sabatini et al. (2019)*) or Spectral Element
415 Methods (SEM, *Brissaud et al. (2017)*; *Martire et al. (2021)*). However, the computational
416 cost associated with such method is much greater than for PE simulations and generating a
417 large synthetic dataset would require extensive computational resources. This cost could be
418 somewhat alleviated since, by resolving the full three-dimensional wavefield, multiple TLs
419 could be extracted from one FD or SEM simulation by considering different azimuths from
420 the source. Once trained over computationally expensive FD or SEM simulations, we can
421 anticipate the cost of one ML simulation to be on the same order than presented here (< 0.1
422 s) which makes ML even more attractive than when trained over PE simulations. As FD or
423 SEM tools can incorporate topography, an encoded representation of topographic variations
424 (e.g., one-dimensional CNN) could be concatenated to the frequency and encoded winds to
425 provide more accurate predictions.

426 This work paves the way for the monitoring and characterization of infrasound sources.
427 Recent studies (*Vorobeva et al., 2021*; *De Carlo et al., 2021*) have shown that infrasound
428 generated by colliding ocean waves, called microbaroms, may provide important constraints
429 on stratospheric winds. To validate their theoretical model connecting ocean sources and
430 observations, these studies rely on the empirical model presented in *Le Pichon et al. (2012)*.
431 Extending the current ML model to longer ranges (> 1000 km) would be critical for global
432 acoustic event analysis, but would also allow an enhanced modelling of microbarom amplitudes,
433 hence also facilitating the development of global infrasound-based near-realtime atmospheric
434 model diagnostics. Similarly, fast and accurate TL predictions would enable the efficient
435 reconstruction of microbarom soundscapes (*den Ouden et al., 2021*), which would enhance
436 our understanding of global infrasonic background noise levels. The localization of infrasound
437 sources is generally performed using only the arrival times and backazimuth observed at ground
438 arrays and neglects amplitude (e.g., *Blom et al. (2018)*). The absence of amplitude inputs
439 in the optimization process owes to the high computational cost of full-waveform modelling
440 approaches. The inexpensive ML model introduced here could enable the exploration

441 of variations of relative amplitudes between stations with the choice of source location.
442 Computationally inexpensive ML modeling would therefore be a great asset for near-real-time
443 monitoring of natural hazards, such as volcanoes, and explosions for the Comprehensive
444 Nuclear-Test-Ban treaty verification.

445 Finally, because ML models provide an analytical relationship between input wind models
446 and ground TLs, our ML tool could be used to investigate the sensitivity of infrasound
447 amplitudes with variations in wind models. Sensitivity kernels could be built using explanatory
448 techniques such as Layer-wise Relevance Propagation (*Bach et al., 2015*) which propagates
449 the ML predictions backwards in the neural network to determine what part of the input
450 data, i.e., wind model, was used to build a given output, i.e., TL. The construction of
451 wind sensitivity kernels could then be employed to further constrain wind structures in
452 infrasound-based wind inversions (*Vera Rodriguez et al., 2020*). While we restricted our
453 model to absolute TL predictions, i.e., predictions of the norm of the complex TL, both real
454 and imaginary parts of the TL could be independently predicted. Predicting complex TL
455 would enable one to reconstruct the full infrasound time series from any source time function
456 input (e.g., *Arrowsmith et al. (2012)*).

457 AUTHOR CONTRIBUTIONS

458 Quentin Brissaud (QB) and Sven Peter Näsholm (SPN) initiated this work and elaborated
459 the plan for the study. QB performed the wave propagation simulations and implemented
460 the ML training and validation. Antoine Turquet (AT) implemented the Gardner’s model in
461 Python. Alexis Le Pichon (ALP) generated the LP12 TL profiles (*Le Pichon et al., 2012*)
462 which are presented in Fig. 5. QB created the figures, which were further elaborated in
463 collaboration with all co-authors. QB wrote the initial manuscript draft and all co-authors
464 contributed in review, revisions, and editing previous to submission.

465 ACKNOWLEDGMENTS

466 The authors would like to thank Alexander Binder and Adín Ramírez Rivera, Associate
467 Professors at the Department of Informatics, University of Oslo, for insightful discussion

468 in the implementation and optimization of Convolutional Neural Networks and transfer
469 learning. The authors are also grateful to Claus Hetzer, Research and Development Engineer
470 at University of Mississippi, for providing details about the theoretical background behind the
471 Parabolic Equations modelling software ePape. The authors are thankful for insightful reviews
472 received from Jelle Assink and an anonymous referee. These have helped us significantly
473 improve the manuscript.

474 This work was mainly funded from a NOR SAR institute grant. It was also supported by
475 the project *Middle Atmosphere Dynamics: Exploiting Infrasonnd Using a Multidisciplinary*
476 *Approach at High Latitudes* (MADEIRA), funded by the Research Council of Norway basic
477 research programme FRIPRO/FRINATEK under Contract No. 274377. This study was
478 facilitated by previous research performed within the framework of the ARISE and ARISE2
479 projects (*Blanc et al.*, 2018, 2019), funded by the European Commission FP7 and Horizon
480 2020 programmes (Grant Nos. 284387 and 653980)

481 **DATA AVAILABILITY STATEMENT**

482 The ERA5 operational data were accessed from the ECMWF MARS archive using the
483 Climate Data Store API (*ECMWF*, 2018), which is accessible to ECMWF Member and
484 Co-operating States. We are grateful to the National Center for Physical Acoustics (NCPA) at
485 the University of Mississippi for making the Parabolic Equation modelling tool ePape publicly
486 available through GitHub at *Waxler et al.* (2021). The TensorFlow library for Python can be
487 downloaded from the TensorFlow repository (<https://doi.org/10.5281/zenodo.4724125>).
488 The ML model Python implementation, and the corresponding PE TL profiles will be released
489 upon publication on a GitHub repository.

490 **REFERENCES**

491 Abadi, M., A. Agarwal, P. Barham, E. Brevdo, Z. Chen, C. Citro, G. S. Corrado, A. Davis,
492 J. Dean, M. Devin, S. Ghemawat, I. Goodfellow, A. Harp, G. Irving, M. Isard, Y. Jia,
493 R. Jozefowicz, L. Kaiser, M. Kudlur, J. Levenberg, D. Mané, R. Monga, S. Moore,
494 D. Murray, C. Olah, M. Schuster, J. Shlens, B. Steiner, I. Sutskever, K. Talwar, P. Tucker,

- 495 V. Vanhoucke, V. Vasudevan, F. Viégas, O. Vinyals, P. Warden, M. Wattenberg, M. Wicke,
496 Y. Yu, and X. Zheng (2015), TensorFlow: Large-scale machine learning on heterogeneous
497 systems, software available from tensorflow.org.
- 498 Arrowsmith, S. J., R. Burlacu, K. Pankow, B. Stump, R. Stead, R. Whitaker, and C. Hayward
499 (2012), A seismoacoustic study of the 2011 january 3 circleville earthquake, *Geophysical*
500 *Journal International*, *189*(2), 1148–1158, doi:10.1111/j.1365-246X.2012.05420.x.
- 501 Averbuch, G., J. D. Assink, and L. G. Evers (2020), Long-range atmospheric infrasound
502 propagation from subsurface sources, *J. Acoust. Soc. Am.*, *147*(2), 1264–1274, doi:
503 10.1121/10.0000792.
- 504 Bach, S., A. Binder, G. Montavon, F. Klauschen, K.-R. Müller, and W. Samek (2015), On
505 pixel-wise explanations for non-linear classifier decisions by layer-wise relevance propagation,
506 *PloS one*, *10*(7), e0130140, doi:10.1371/journal.pone.0130140.
- 507 Blanc, E., L. Ceranna, A. Hauchecorne, A. Charlton-Perez, E. Marchetti, L. Evers, T. Kvaerna,
508 J. Lastovicka, L. Eliasson, N. Crosby, P. Blanc-Benon, A. Le Pichon, N. Brachet, C. Pilger,
509 P. Keckhut, J. Assink, P. M. Smets, C. Lee, J. Kero, T. Sindelarova, N. Kämpfer,
510 R. Rüfenacht, T. Farges, C. Millet, S. Näsholm, S. Gibbons, P. Espy, R. Hibbins, P. Heinrich,
511 M. Ripepe, S. Khaykin, N. Mze, and J. Chum (2018), Toward an improved representation
512 of middle atmospheric dynamics thanks to the ARISE project, *Surveys in Geophysics*,
513 *39*(2), 171–225, doi:10.1007/s10712-017-9444-0.
- 514 Blanc, E., K. Pol, A. Le Pichon, A. Hauchecorne, P. Keckhut, G. Baumgarten, J. Hildebrand,
515 J. Höffner, G. Stober, R. Hibbins, P. Espy, M. Rapp, B. Kaifler, L. Ceranna, P. Hupe,
516 J. Hagen, R. Rüfenacht, N. Kämpfer, and P. Smets (2019), Middle atmosphere variability
517 and model uncertainties as investigated in the framework of the arise project, in *Infrasound*
518 *Monitoring for Atmospheric Studies*, pp. 845–887, Springer.
- 519 Blom, P. S., F. K. Dannemann, and O. E. Marcillo (2018), Bayesian characterization
520 of explosive sources using infrasonic signals, *Geophysical Journal International*, *215*(1),
521 240–251, doi:10.1093/gji/ggy258.
- 522 Brissaud, Q., R. Martin, R. F. Garcia, and D. Komatitsch (2016), Finite-difference numerical
523 modelling of gravitoacoustic wave propagation in a windy and attenuating atmosphere,
524 *Geophys. J. Int.*, *206*(1), 308–327.

- 525 Brissaud, Q., R. Martin, R. F. Garcia, and D. Komatitsch (2017), Hybrid galerkin numerical
526 modelling of elastodynamics and compressible navier–stokes couplings: applications to
527 seismo-gravito acoustic waves, *Geophys. J. Int.*, *210*(2), 1047–1069, doi:10.1093/gji/ggx185.
- 528 Brissaud, Q., S. Krishnamoorthy, J. M. Jackson, D. C. Bowman, A. Komjathy, J. A. Cutts,
529 Z. Zhan, M. T. Pauken, J. S. Izraelevitz, and G. J. Walsh (2021), The first detection of
530 an earthquake from a balloon using its acoustic signature, *Geophysical Research Letters*,
531 *48*(12), e2021GL093013, doi:10.1029/2021GL093013.
- 532 Ceranna, L., A. Le Pichon, D. Green, and P. Mialle (2009), The buncefield explosion: a
533 benchmark for infrasound analysis across central europe, *Geophysical Journal International*,
534 *177*(2), 491–508, doi:10.1111/j.1365-246X.2008.03998.x.
- 535 Chunchuzov, I., and S. Kulichkov (2019), Internal gravity wave perturbations and their
536 impacts on infrasound propagation in the atmosphere, in *Infrasound Monitoring for*
537 *Atmospheric Studies*, pp. 551–590, Springer, doi:10.1007/978-3-319-75140-5_16.
- 538 Chunchuzov, I., S. Kulichkov, V. Perepelkin, O. Popov, P. Firstov, J. Assink, and E. Marchetti
539 (2015), Study of the wind velocity-layered structure in the stratosphere, mesosphere, and
540 lower thermosphere by using infrasound probing of the atmosphere, *Journal of Geophysical*
541 *Research: Atmospheres*, *120*(17), 8828–8840, doi:10.1002/2015JD023276.
- 542 d’Ascoli, S., L. Sagun, G. Biroli, and J. Bruna (2019), Finding the needle in the haystack
543 with convolutions: on the benefits of architectural bias, *Advances in Neural Information*
544 *Processing Systems*, *32*.
- 545 De Carlo, M., P. Hupe, A. Le Pichon, L. Ceranna, and F. Arduin (2021), Global microbarom
546 patterns: a first confirmation of the theory for source and propagation, *Geophysical Research*
547 *Letters*, *48*(3), e2020GL090163, doi:10.1029/2020GL090163.
- 548 de Groot-Hedlin, C. (2008), Finite-difference time-domain synthesis of infrasound propagation
549 through an absorbing atmosphere, *The Journal of the Acoustical Society of America*, *124*(3),
550 1430–1441, doi:10.1121/1.2959736.
- 551 de Groot-Hedlin, C. D., M. A. Hedlin, and D. P. Drob (2010), Atmospheric variability and
552 infrasound monitoring, in *Infrasound Monitoring for Atmospheric Studies*, pp. 475–507,
553 Springer, doi:10.1007/978-1-4020-9508-5_15.

- 554 den Ouden, O. F., P. S. Smets, J. D. Assink, and L. G. Evers (2021), A bird’s-eye view on
555 ambient infrasonic soundscapes, *Geophysical Research Letters*, *48*(17), e2021GL094555,
556 doi:10.1029/2021GL094555.
- 557 Deng, J., W. Dong, R. Socher, L.-J. Li, K. Li, and L. Fei-Fei (2009), Imagenet: A large-scale
558 hierarchical image database, in *2009 IEEE conference on computer vision and pattern*
559 *recognition*, pp. 248–255, Ieee, doi:10.1109/CVPR.2009.5206848.
- 560 Drob, D. P., J. Picone, and M. Garcés (2003), Global morphology of infrasound propagation,
561 *Journal of Geophysical Research: Atmospheres*, *108*(D21), doi:10.1029/2002JD003307.
- 562 Drob, D. P., D. Broutman, M. A. Hedlin, N. W. Winslow, and R. G. Gibson (2013), A
563 method for specifying atmospheric gravity wavefields for long-range infrasound propagation
564 calculations, *Journal of Geophysical Research: Atmospheres*, *118*(10), 3933–3943, doi:
565 <https://doi.org/10.1029/2012JD018077>.
- 566 Drob, D. P., J. T. Emmert, J. W. Meriwether, J. J. Makela, E. Doornbos, M. Conde,
567 G. Hernandez, J. Noto, K. A. Zawdie, S. E. McDonald, J. D. Huba, and J. H. Klenzing
568 (2015), An update to the horizontal wind model (HWM): The quiet time thermosphere,
569 *Earth and Space Science*, *2*(7), 301–319, doi:<https://doi.org/10.1002/2014EA000089>.
- 570 ECMWF (2018), Era5 model level, <https://cds.climate.copernicus.eu/>.
- 571 Evers, L. G., and H. W. Haak (2010), The characteristics of infrasound, its propagation and
572 some early history, in *Infrasound monitoring for atmospheric studies*, pp. 3–27, Springer,
573 doi:10.1007/978-1-4020-9508-5_1.
- 574 Fee, D., and R. S. Matoza (2013), An overview of volcano infrasound: From hawaiian to
575 plinian, local to global, *Journal of Volcanology and Geothermal Research*, *249*, 123–139,
576 doi:10.1016/j.jvolgeores.2012.09.002.
- 577 Fee, D., R. Waxler, J. Assink, Y. Gitterman, J. Given, J. Coyne, P. Mialle, M. Garces, D. Drob,
578 D. Kleinert, et al. (2013), Overview of the 2009 and 2011 sayarim infrasound calibration
579 experiments, *Journal of Geophysical Research: Atmospheres*, *118*(12), 6122–6143.
- 580 Gardner, C. S., C. A. Hostetler, and S. J. Franke (1993), Gravity wave models for the
581 horizontal wave number spectra of atmospheric velocity and density fluctuations, *Journal*
582 *of Geophysical Research: Atmospheres*, *98*(D1), 1035–1049, doi:10.1029/92JD02051.

- 583 Glorot, X., and Y. Bengio (2010), Understanding the difficulty of training deep feedforward
584 neural networks, in *Proceedings of the thirteenth international conference on artificial*
585 *intelligence and statistics*, pp. 249–256, JMLR Workshop and Conference Proceedings.
- 586 Golden, P., P. Negraru, and J. Howard (2012), Infrasound studies for yield estimation of HE
587 explosions, *Tech. rep.*, Southern Methodist University, Dallas Texas.
- 588 Hart, C. R., D. K. Wilson, C. L. Pettit, and E. T. Nykaza (2021), Machine-learning of
589 long-range sound propagation through simulated atmospheric turbulence, *The Journal of*
590 *the Acoustical Society of America*, 149(6), 4384–4395, doi:10.1121/10.0005280.
- 591 He, K., X. Zhang, S. Ren, and J. Sun (2016), Deep residual learn-
592 ing for image recognition, in *Proceedings of the IEEE conference*
593 *on computer vision and pattern recognition*, pp. 770–778, doi:
594 https://openaccess.thecvf.com/content_cvpr_2016/html/He_Deep_Residual_Learning_CVPR_2016
- 595 Head, T., M. Kumar, H. Nahrstaedt, G. Louppe, and I. Shcherbatyi (2021), scikit-
596 optimize/scikit-optimize, doi:10.5281/zenodo.5565057, last accessed on 29 October 2021.
- 597 Hernandez, B., A. Le Pichon, J. Vergoz, P. Herry, L. Ceranna, C. Pilger, E. Marchetti,
598 M. Ripepe, and R. Bossu (2018), Estimating the ground-motion distribution of the 2016
599 mw 6.2 amatrice, italy, earthquake using remote infrasound observations, *Seismol. Res.*
600 *Lett.*, 89(6), 2227–2236, doi:10.1785/0220180103.
- 601 Ioffe, S., and C. Szegedy (2015), Batch normalization: Accelerating deep network training
602 by reducing internal covariate shift, in *Proceedings of the 32nd International Conference*
603 *on International Conference on Machine Learning - Volume 37*, ICML’15, p. 448–456,
604 JMLR.org, doi:10.5555/3045118.3045167.
- 605 Kingma, D. P., and J. Ba (2015), Adam: A method for stochastic optimization, in *3rd*
606 *International Conference on Learning Representations, ICLR 2015, San Diego, CA, USA,*
607 *May 7-9, 2015, Conference Track Proceedings*, edited by Y. Bengio and Y. LeCun, doi:
608 arXiv:1412.6980v9.
- 609 Krizhevsky, A., I. Sutskever, and G. E. Hinton (2012), Imagenet classification with deep
610 convolutional neural networks, *Advances in neural information processing systems*, 25,
611 1097–1105, doi:10.1145/3065386.

- 612 Kumar, G. K., K. K. Kumar, G. Baumgarten, and G. Ramkumar (2015), Validation
613 of MERRA reanalysis upper-level winds over low latitudes with independent rocket
614 sounding data, *Journal of Atmospheric and Solar-Terrestrial Physics*, *123*, 48–54, doi:
615 10.1016/j.jastp.2014.12.001.
- 616 Lai, V. H., Z. Zhan, Q. Brissaud, O. Sandanbata, and M. S. Miller (2021), Inflation
617 and asymmetric collapse at kilauea summit during the 2018 eruption from seismic and
618 infrasound analyses, *Journal of Geophysical Research: Solid Earth*, p. e2021JB022139,
619 doi:10.1029/2021JB022139.
- 620 Lalande, J.-M., and R. Waxler (2016), The interaction between infrasonic waves and gravity
621 wave perturbations: Application to observations using uttr rocket motor fuel elimina-
622 tion events, *Journal of Geophysical Research: Atmospheres*, *121*(10), 5585–5600, doi:
623 <https://doi.org/10.1002/2015JD024527>.
- 624 Le Pichon, A., L. Ceranna, and J. Vergoz (2012), Incorporating numerical modeling into
625 estimates of the detection capability of the ims infrasound network, *Journal of Geophysical*
626 *Research: Atmospheres*, *117*(D5), doi:10.1029/2011JD016670.
- 627 Martire, L., R. Martin, Q. Brissaud, and R. Garcia (2021), Specfem2d-dg, an open source
628 software modeling mechanical waves in coupled solid-fluid systems: the linearised navier-
629 stokes approach, *Geophysical Journal International*, doi:10.1093/gji/ggab308.
- 630 Michalopoulou, Z.-H., P. Gerstoft, B. Kostek, and M. A. Roch (2021), Introduction to the
631 special issue on machine learning in acoustics, *The Journal of the Acoustical Society of*
632 *America*, *150*(4), 3204–3210, doi:10.1121/10.0006783.
- 633 Norris, D., and R. Gibson (2002), Inframap enhancements: environmental/propagation
634 variability and localization accuracy of infrasonic networks, in *Proceedings of the 24th*
635 *Seismic Research Review—Nuclear Explosion Monitoring: Innovation and Integration*, pp.
636 809–813.
- 637 Pettit, C. L., and D. K. Wilson (2020), A physics-informed neural network for sound
638 propagation in the atmospheric boundary layer, in *Proceedings of Meetings on Acoustics*
639 *179ASA*, vol. 42, p. 022002, Acoustical Society of America, doi:10.1121/2.0001383.
- 640 Picone, J., A. Hedin, D. P. Drob, and A. Aikin (2002), NRLMSISE-00 empirical model of the
641 atmosphere: Statistical comparisons and scientific issues, *Journal of Geophysical Research:*

- 642 *Space Physics*, 107(A12), SIA–15, doi:10.1029/2002JA009430.
- 643 Raissi, M., P. Perdikaris, and G. E. Karniadakis (2019), Physics-informed neural net-
644 works: A deep learning framework for solving forward and inverse problems involving
645 nonlinear partial differential equations, *Journal of Computational Physics*, 378, 686–707,
646 doi:10.1016/j.jcp.2018.10.045.
- 647 Sabatini, R., O. Marsden, C. Bailly, and O. Gainville (2019), Three-dimensional direct
648 numerical simulation of infrasound propagation in the earth’s atmosphere, *Journal of Fluid*
649 *Mechanics*, 859, 754–789, doi:10.1017/jfm.2018.816.
- 650 Shani-Kadmiel, S., G. Averbuch, P. Smets, J. Assink, and L. Evers (2021), The 2010 haiti
651 earthquake revisited: An acoustic intensity map from remote atmospheric infrasound obser-
652 vations, *Earth and Planetary Science Letters*, 560, 116,795, doi:10.1016/j.epsl.2021.116795.
- 653 Simonyan, K., and A. Zisserman (2015), Very deep convolutional networks for large-scale
654 image recognition, in *3rd International Conference on Learning Representations, ICLR*
655 *2015, San Diego, CA, USA, May 7-9, 2015, Conference Track Proceedings*, edited by
656 Y. Bengio and Y. LeCun.
- 657 Sutherland, L. C., and H. E. Bass (2004), Atmospheric absorption in the atmosphere
658 up to 160 km, *The Journal of the Acoustical Society of America*, 115(3), 1012–1032,
659 doi:10.1029/2006JD007806.
- 660 Tailpied, D., A. L. Pichon, and B. Taisne (2021), Assessing uncertainties in infrasound
661 network performance modelling: application to the Euro-Mediterranean and Southeast
662 Asian region, *Geophysical Journal International*, doi:10.1093/gji/ggab399, ggab399.
- 663 Vera Rodriguez, I., S. P. Näsholm, and A. Le Pichon (2020), Atmospheric wind and
664 temperature profiles inversion using infrasound: an ensemble model context, *J. Acoust.*
665 *Soc. Am.*, 148(5), 2923–2934, doi:10.1121/10.0002482.
- 666 Vergoz, J., A. L. Pichon, and C. Millet (2019), The Antares explosion observed by the
667 USArray: An unprecedented collection of infrasound phases recorded from the same event,
668 in *Infrasound monitoring for atmospheric studies*, pp. 349–386, Springer.
- 669 Vorobeva, E., M. D. Carlo, A. L. Pichon, P. J. Espy, and S. P. Näsholm (2021), Benchmarking
670 microbarom radiation and propagation model against infrasound recordings: a vespagram-
671 based approach, *Annales Geophysicae*, 39, 515–531, doi:10.5194/angeo-39-515-2021.

672 Waxler, R., C. Hetzer, J. Assink, and D. Velea (2021), chetzer-ncpa/ncpaprop-release:
673 Ncpaprop v2.1.0, doi:10.5281/zenodo.5562713, last accessed on 29 October 2021.

674 Zhuang, F., Z. Qi, K. Duan, D. Xi, Y. Zhu, H. Zhu, H. Xiong, and Q. He (2020), A
675 comprehensive survey on transfer learning, *Proceedings of the IEEE*, 109(1), 43–76, doi:
676 10.1109/JPROC.2020.3004555.

677 **Appendix A: Hyper-parameter optimization**

678 The ML model is described by a set of hyper-parameters that must be optimized in order
679 to obtain the best regression performance. First, we optimized the ML architecture, i.e.,
680 the number of CNN and dense layers as well as number of CNN filters, using a Bayesian
681 optimization with Gaussian Processes as implemented in the scikit-optimize Python library
682 (*Head et al.*, 2021). In addition to architecture optimizations, we investigated the variations
683 in RMSE with the choice of training parameters (batch size and validation dataset size) as
684 well as inputs image size. Such variations are shown in Fig. 7. There are generally negligible
685 error differences between each model. As a trade-off between training time and error we
686 choose batches of size 32, a dataset of size 20%, and input images of size 20×4 .

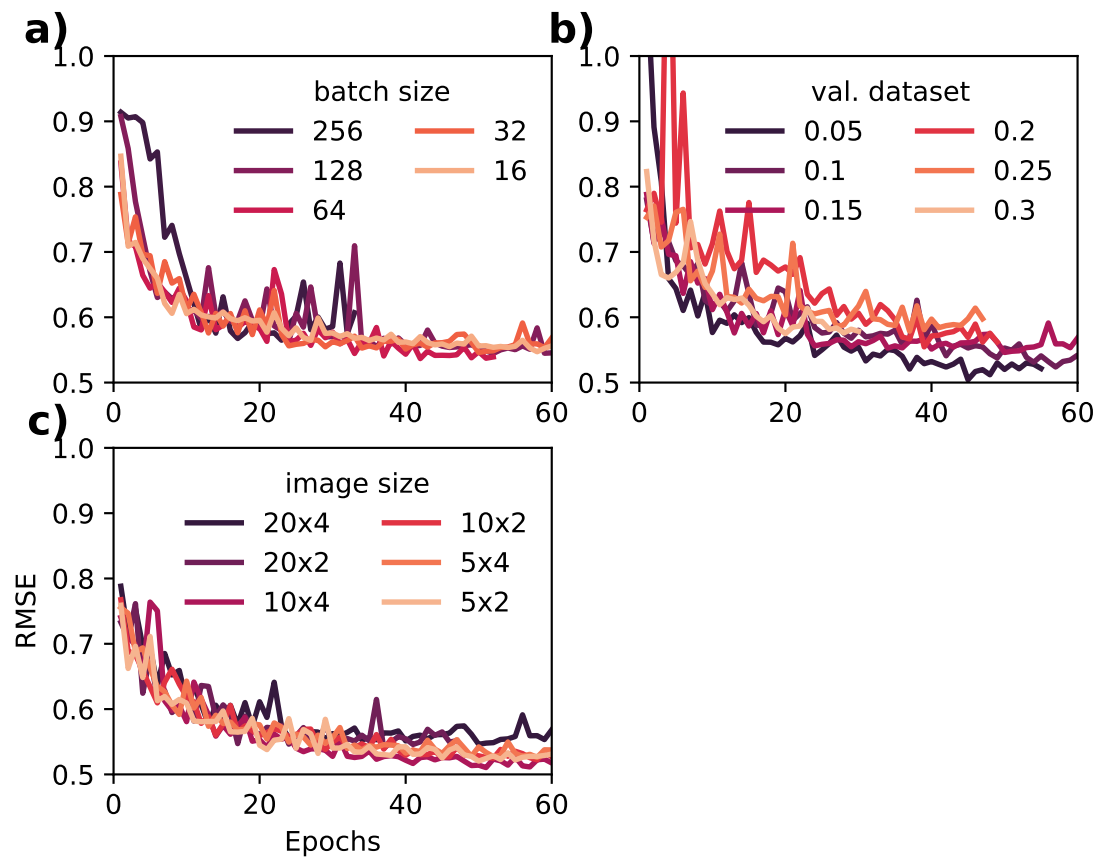


Figure 7. Optimization of training and input hyperparameters. RMSE vs epochs during training for variations in (a) batch size, (b) validation dataset size, and (c) input image size from a baseline model with: batch size 32, 15% validation dataset size, and 20×4 input size.